applied sciences

MDPI

Article

A Novel Sensorless Approach for Speed and Displacement Control of Bearingless Switched Reluctance Motor

Pulivarthi Nageswara Rao [1], Nallapaneni Manoj Kumar [2,*], Sanjeevikumar Padmanaban [3,*], M. S. P. Subathra [4] and Aneesh A. Chand [5]

1 Department of Electrical Electronics and Communication Engineering, Gandhi Institute of Technology and Management (Deemed to be University), Visakhapatnam 530045, Andhra Pradesh, India; dr.nageshpulivarthi@gmail.com or nagesh.pulivarthi@gitam.edu
2 School of Energy and Environment, City University of Hong Kong, Kowloon, Hong Kong, China
3 Department of Energy Technology, Aalborg University, 6700 Esbjerg, Denmark
4 Department of Electrical and Electronics Engineering, Karunya Institute of Technology and Sciences, Coimbatore 641114, Tamil Nadu, India; subathra@karunya.edu
5 School of Engineering and Physics, The University of the South Pacific, Suva, Fiji; aneeshamitesh@gmail.com
* Correspondence: nallapanenichow@gmail.com or mnallapan2-c@my.cityu.edu.hk (N.M.K.); san@et.aau.dk (S.P.)

Received: 2 May 2020; Accepted: 9 June 2020; Published: 12 June 2020

Abstract: The bearingless concept is a plausible alternative to the magnetic bearing drives. It provides numerous advantages like minimal maintenance, low cost, compactness and no requirement of high-performance power amplifiers. Controlling the rotor position and its displacements under parameter variations during acceleration and deceleration phases was not effective with the use of conventional controllers like proportional–integral–derivative (PID) and fuzzy-type controllers. Hence, to get the robust and stable operation of a bearingless switched reluctance motor (BSRM), a new robust dynamic sliding mode controller has been proposed in this paper, along with a sensorless operation using a sliding ode observer. The rotor displacement tracking error functions and speed tracking error functions are used in the designing of both proposed methods of the sliding mode switching functions. To get a healthy and stable operation of the BSRM, the proposed controller's tasks are divided into three steps. As a first step, the displaced rotor in any one of the four quadrants in the air gap has to pull back to the centre position successfully. The second step is to run the motor at a rated speed by exciting torque phase currents, and finally, the third step is to maintain the stable and robust operation of the BSRM even under the application of different loads and changes of the motor parameters. Simulation studies were conducted and analysed under different testing conditions. The suspension forces, rotor displacements, are robust and stable, and the rotor is pulled back quickly to the centre position due to the proposed controller's actions. The improved performance characteristics of the dynamic sliding mode controller (DSMC)-based sliding mode observer (SMO) was compared with the conventional sliding mode controller (SMC)-based SMO.

Keywords: asymmetric converter; bearingless; dynamic sliding mode control; sensorless; sliding mode observer

1. Introduction

The high-speed motors operating in adverse locations involving high temperatures are often prone to motor breakdown. According to recent surveys, nearly 51% of motor breakdowns are only due to bearing failures, which result in the shutdown of industrial process involving electric drives.

The subsequent motor-bearing failures may affect modern industrial progress, causing undesirable and unreliable conditions. Solving motor bearing breakdowns became the most challenging task for researchers for a decade. Extensive research has been going on developing bearingless technology by eliminating the conventional mechanical-bearing system.

The bearingless concept is a plausible alternative to the magnetic bearing drives, as it provides numerous advantages like minimal maintenance, low cost, compactness and redundant, high-performance power amplifiers [1–3]. Compared with conventional switched reluctance motors, the levitation of the rotor at the centre point and suspension force control is an additional task for bearingless switched reluctance motors (BSRMs). Besides stable rotor suspension control of the BSRM, there exists another duty in controlling the rotor position and its displacement under parameter variations during acceleration and deceleration phases.

The perfect realisation of the BSRM is difficult to simulate and control due to its nonlinear magnetisation characteristics. For these reasons, the BSRM will not be used in high-precision and high-performance industrial applications. Apart from the difficulty of the model, the BSRM should operate in a continuous phase-to-phase switching mode for basic motor workings [4–6]. Therefore, various complex controllers are required to realise the full potential of the BSRM and to overcome its drawbacks, as mentioned above. Hence, to get less rotor eccentric displacements and steady speed and torque profiles of the BSRM, a new robust controller, i.e., dynamic sliding mode controller (DSMC), is proposed in this paper.

The DSMC has received considerable attention due to its dynamic properties. The DSMC provides asymptotic stability to the states of tracking error dynamics and stability to the internal states. The sliding manifold with a new dynamic is called a DSMC. The DSMC improves the order of the system by number. Further, the designed compensators may not only enhance the stability of the sliding system but, also, improve the desired characteristics and performance of the system [7,8].

Practically at high speeds, the accurate controlling of the rotor position and its displacement through the sensors makes it unfair, and this setup will increase the space, cost and complexity in the controlling process [9–11]. Hence, in recent days, various direct and indirect sensorless methods are applied to BSRM drives. To avoid the mechanical sensors and to get accurate rotor position information, sliding mode observer (SMO)-based sensorless speed and displacement control technics are presented in this paper. The rotor displacement tracking error functions and speed error tracking functions are considered in the designing of the switching surface for the proposed dynamic sliding mode control.

To get a healthy and stable operation of the BSRM, the proposed controller's tasks are divided into three steps. As the first step, the displaced rotor in any one of the four quadrants in the air gap has to pull back to the centre position successfully. The second step is to run the motor at a rated speed by exciting the torque phase currents, and finally, the third step is to maintain the stable and robust operation of the BSRM even under the application of different loads and changes of the motor parameters. Improved rotor displacement and speed controllers are proposed to the model derived for the existing 12/14 BSRM. The issues like modelling, simulation, control without position and displacement sensors, the implementation of a robust controller and observers are the significant contributions of this paper. The proposed control methods have to achieve a quick and hassle-free start and better control actions on rotor displacement and speed. Such control schemes offer higher accuracy in sensorless operations for a wide speed range and help to reduce the torque ripple of the drive appreciably.

The article is structured as follows: Section 2 briefly described the operation and modelling of the BSRM. In Section 3, the modelling of the proposed controller and observer is given. Results and discussion are presented in Section 4, the detailed comparison of the proposed controller is presented in Section 5. Lastly the conclusions were drawn and presented in Section 6.

2. Operation and Modelling of the Bearingless Switched Reluctance Motor

2.1. Operating Principle

The BSRM has salient poles both in the rotor and stator, and the excitation is limited to stator windings only. The excitation currents are unidirectional and discontinuous. The stator phases are sequentially excited to obtain continuous rotation [12–14]. Hence, the design of the controllers for the BSRM is more complicated due to its nonlinear magnetic field distribution. The basic 12/14 BSRM salient pole structure is illustrated in Figure 1. Two regulated individual DC voltages are given to the suspension and torque coils to realise the decoupled performance between the net suspension winding's force and main winding's torque. The suspension winding coils Is1 and Is3 produce the radial force in the Y-directional, and coils Is2 and Is4 produce the radial force in the X-directional. Positive suspension forces are produced from Is2 and Is1; similarly, Is4 and Is3 poles produce negative suspension forces. The resultant rotational torque will be produced from the stator main phase coils called phase-A and phase-B. The operating parameters and ratings of the 12/14 BSRM are given in Table 1.

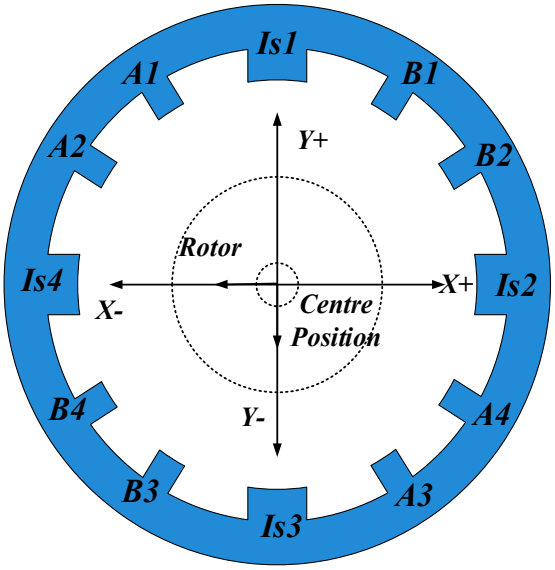

Figure 1. Structure and winding pattern of the stator.

Table 1. Operating details of the 12/14 bearingless switched reluctance motor (BSRM).

Parameters	Value
Rated power(motor)	1 kW
Maximum motor Current/phase	4 amp
Voltage/phase	250 volts
Net torque	1 Nm
Speed	9000 rpm
Toque winding per phase resistance	0.86 ohms
Suspension winding per phase resistance	0.32 ohms
Suspension voltage	250 volts
Maximum suspension current	4 amp

Hence, the BSRM drive needs a total of six hysteresis controllers to regulate both the suspension force and torque. Out of six, two are used as individual phase current controllers, and the remaining four suspension force current controllers are used to control the suspension currents. The suspension force pole arc is carefully chosen not to be less than one-rotor pole pitch to maintain the continuous levitation force. Therefore, the pole arcs of both the suspension pole and rotor pole are equal in dimensions.

2.2. Rotor Modelling (Suspension Control)

The suspension forces required for the levitation of the rotor in both the X and Y directions are given below at the standstill position:

$$Fx = m\frac{d^2x}{dt^2} + kx \tag{1}$$

$$Fy = m\frac{d^2y}{dt^2} + ky + mg \tag{2}$$

Here, X_1, X_2, Y_1 and Y_2 are chosen as the state variables from Equations (1) and (2). Hence, the desired tracking rotor displacement states are modelled as:

$$\begin{gathered} \dot{X}_1 = X_2 \; ; \; \dot{Y}_1 = Y_2 \\ \dot{X}_2 = -\frac{k_x}{m}X_1 + \frac{F_x}{m} + F_{dx} \; ; \; \dot{Y}_2 = -\frac{k_y}{m}Y_1 + \frac{F_y}{m} + F_{dy} + g \end{gathered} \tag{3}$$

The net suspending forces produced in the X-Y directions are written in electrical equivalence, as given in Equation (4):

$$\begin{bmatrix} F_x \\ F_y \end{bmatrix} = \begin{bmatrix} K_{xxp} & K_{xyp} & K_{xxn} & K_{xyn} \\ K_{yxp} & K_{yyp} & K_{yxn} & K_{yyn} \end{bmatrix} \begin{bmatrix} {i_{xp}}^2 \\ {i_{yp}}^2 \\ {i_{xn}}^2 \\ {i_{xn}}^2 \end{bmatrix} \tag{4}$$

By equating the above Equations (3) and (4), we get the following Equations (5) and (6):

$$F_x = m\frac{d^2x}{dt^2} + kx = [K_X][I_x] \tag{5}$$

$$Fy = m\frac{d^2y}{dt^2} + ky + mg = [K_Y][I_Y] \tag{6}$$

where $K_X = diag\begin{bmatrix} Kxxp & Kxyp & Kxxn & kxyn \end{bmatrix}$, $K_Y = diag\begin{bmatrix} Kyxp & Kyyp & Kyxn & Kyyn \end{bmatrix}$ and $I_x = \begin{bmatrix} {I_{xp}}^2 \\ {I_{xn}}^2 \end{bmatrix}$ and $I_Y = \begin{bmatrix} {I_{yp}}^2 \\ {I_{yn}}^2 \end{bmatrix}$.

The equivalent desired tracking state space equations for rotor displacements are given as follows in Equation (7):

$$\begin{bmatrix} \dot{X}_1 \\ \dot{X}_2 \\ \dot{Y}_1 \\ \dot{Y}_2 \end{bmatrix} = \begin{bmatrix} 1 & 0 & 0 & 0 \\ -\frac{k}{m} & 0 & 0 & 0 \\ 0 & 0 & 1 & 0 \\ 0 & 0 & -\frac{k}{m} - g & 0 \end{bmatrix} \begin{bmatrix} X_1 \\ X_2 \\ Y_1 \\ Y_2 \end{bmatrix} + \begin{bmatrix} 0 & 0 & 0 & 0 \\ Kxxp & Kxyp & Kxxn & Kxyn \\ 0 & 0 & 0 & 0 \\ Kyxp & Kyyp & Kyxn & Kyyn \end{bmatrix} \times \begin{bmatrix} {i_{xp}}^2 \\ {i_{yp}}^2 \\ {i_{xn}}^2 \\ {i_{xn}}^2 \end{bmatrix} \tag{7}$$

2.3. The Speed Control of the BSRM

The flux linkages vector "Ψ", the voltage vector "V", the phase current vector "i", the vector of the mutual inductance matrix "N" and phase resistances "r" are the modelled state space to get the perfect realisation of the BSRM and are given in Equation (8):

$$\frac{d\Psi}{dt} = -rN(\theta)\Psi + V + w_\Psi; \; \frac{dw}{dt} = \frac{T_e - T_l}{J} - \frac{B}{J}w + \frac{T_e}{J} + w_w; \; \frac{d\theta}{dt} = w + w_\theta \text{ and } i = N(\theta)\Psi \tag{8}$$

2.4. Switching Control Strategy

The 12/14 bearingless SRM drive system only needs 12 power switches. As discussed in the operating principle, the 12/14 BSRM is total a six-phase drive. Therefore, eight power switches are required for controlling the four-phase suspension windings, and four power switches are required for the two-phase torque winding control. The topology of the asymmetric converter circuit is shown below in Figure A1 (in Appendix A.1). The detailed switch numbers are given in Table 2.

Table 2. Switch numbers for the 12/14 bearingless switched reluctance motor (BSRM).

12/14 BSRM	Number of Power Switches	Total
Torque winding (two-phase)	2 per phase	4
Suspending force winding (four-phase/four poles)	2 per pole	8

Figure 2 shows the overall independent suspension control switching scheme diagram of the BSRM. The selection of suspending force windings is mentioned in Table 3. From Table 3, the switching state 1 indicates the magnetisation mode and the switching state 0 means the freewheeling mode.

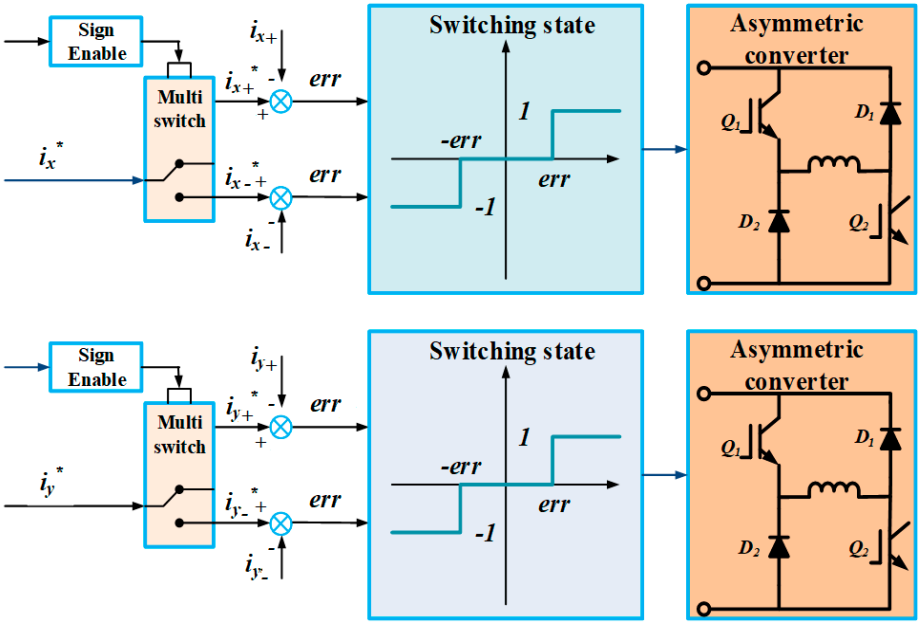

Figure 2. Switching states of the hysteresis control method.

Table 3. Switching state rule of the hysteresis control method for the bearingless switched reluctance motor (BSRM).

Desired Force	Suspending Force Poles Selection	Enable Is1	Enable Is2	Enable Is3	Enable Is4
If $F_x \geq 0, F_y \geq o$	Is1 and Is2	1	1	0	0
If $F_x \geq 0, F_y \leq o$	Is2 and Is3	0	1	1	0
If $F_x \leq 0, F_y \leq o$	Is3 and Is4	0	0	1	1
If $F_x \leq 0, F_y \geq o$	Is4 and Is1	1	0	0	1

Note: F_x and F_y are suspension forces in X and Y directions; Is1, Is2, Is3, and Is4 are the suspension winding coils.

3. Modelling of the Proposed Controller and Observer

3.1. Design of the DSMC

Generally, the conventional sliding mode controller (SMC) uses a practically high value of gains to slide the trajectories on the predetermined sliding mode surface [15,16]. The key advantage of the SMC is its robustness, and it does not allow the parametric variations when the system states are on the switching surface. Furthermore, the sliding mode condition can be reached in finite time due to its noncontinuous control law function. However, the SMC at high speeds has drawbacks such as chattering and the steady-state error due to its high switching gains [17,18]. These particular attributes make the SMC less attractive to the bearingless drives, even though it offers robust and stable activities.

To avoid the prominent problems of reaching time and the chattering in the control scheme of the SMC, a new dynamic sliding mode control (DSMC) is implemented. The DSMC guarantees the system robustness and disturbance rejection capability [19,20]. The main features of the dynamic sliding mode controller are given by:

(a) The system will achieve stability even with incomplete information from the state observer or absence of the state observer.
(b) The system will get stability even under the accommodation of unmatched disturbances.
(c) The chattering can be reduced to a great extent.

Defining the state tracking errors and the switching functions are $e_x = \mathrm{x} - \mathrm{x}_d$, $e_y = y - y_d$, $S_x = (C_x \times e_x) + \dot{e}_x$ and $S_y = (C_y \times e_y) + \dot{e}_y$, respectively, where $C_x > 0$ and $C_y > 0$, and it must be Hurwitz. The first-order derivative of the switching functions is given by:

$$\dot{S}_x = C_x \dot{e}_x + \left\{ \frac{-k_x}{m} X_1 + \frac{F_x}{m} + F_{dx} - \dot{X}_d \right\}; \; \dot{S}_y = C_y \dot{e}_x + \left\{ \frac{-k_y}{m} y_1 + \frac{F_y}{m} + F_{dy} + g - \dot{Y}_d \right\} \tag{9}$$

where $\dot{e}_x = \dot{x} - \dot{x}_d$ and $\dot{e}_y = \dot{y} - \dot{y}_d$ (the design of C_x and C_y are given in Appendix A.2.1).

The new dynamic sliding mode switching functions are given by $\sigma_x = \dot{S}_x + \lambda_x S_x$ and $\sigma_y = \dot{S}_y + \lambda_y S_y$ ($\lambda_x > 0$ and $\lambda_y > 0$). When $\sigma_x = 0$ and $\sigma_y = 0$, $\dot{S}_x + \lambda_x S_x = 0$ and $\dot{S}_y + \lambda_y S_y = 0$ are asymptotically stable; therefore, the error and its first-order differential functions tend to zero. (The design of λ_x and λ_y are given in Appendix A.2.2).

The stability analysis is given as follows from the above Equations (10) and (11):

$$\sigma_x = \dot{S}_x + \lambda_x S_x = C_x \dot{e}_x + \left\{ \frac{-k_x}{m} X_1 + \frac{F_x}{m} + F_{dx} - \dot{X}_d \right\} + \lambda_x S_x \tag{10}$$

$$\sigma_y = \dot{S}_y + \lambda_y S_y = C_y \dot{e}_y + \left\{ \frac{-k_y}{m} y_1 + \frac{F_y}{m} + F_{dy} + g - \dot{Y}_d \right\} + \lambda_y S_y \tag{11}$$

Therefore, the rotor X and Y displacement control equations are given by Equations (12) and (13):

$$\dot{U}_x = m\left\{ \frac{-k_x}{m} \dot{x}_2 + (C_x + \lambda_x) \ddot{x}_d + \dddot{x}_d - \left(\frac{C_x}{m} + \frac{\lambda_x}{m} \right) u_x - (C_x + \lambda_x) \left(\frac{-k_x}{m} x_2 \right) - \lambda_x C_x \dot{e}_x - \eta_x sgn(\sigma_x) \right\} \tag{12}$$

$$\dot{U}_y = m\left\{ \frac{-k_y}{m} \dot{y}_2 + \left(C_y + \lambda_y\right) \ddot{y}_d + \dddot{y}_d - \left(\frac{C_y}{m} + \frac{\lambda_y}{m} \right) u_y - \left(C_y + \lambda_y\right) \left(\frac{-k_y}{m} y_2 \right) - \lambda_y C_y \dot{e}_y - \eta_y sgn\left(\sigma_y\right) \right\} \tag{13}$$

The above dynamic feedback controller Equations (12) and (13) guarantee the asymptotic convergence of rotor displacements X_2 and Y_2 to their desired values as t tends to infinity (the designs of σ_x, and σ_y, are given in Appendix A.2.2).

The motor speed tracking control dynamics based on $e_w = \mathrm{w} - w_d$, $\dot{e}_w = \dot{w} - \dot{w}_d$, $\sigma_w = \dot{S}_w + \lambda_w S_w$ and $\lambda \supset 0$ are given as shown in Equation (14).

$$\dot{U}_w = m\left\{\frac{-\dot{B}_w}{J} + (C_w + \lambda_w)\ddot{w}_d + \ddot{w}_d - \left(\frac{C_w}{J} + \frac{\lambda_w}{J}\right) - B_w - (C_w + \lambda_w)\left(\frac{-B_w}{J}\right) - \lambda_w C_w \dot{e}_w - \eta_w sgn(\sigma_w)\right\} \quad (14)$$

Here, C_w and λ_w are the properly chosen positive design parameters. The stepwise procedure and block diagram for the implementation of the designed DSMC for the BSRM is shown in Figures 3 and 4. The design parameters of the DSMC speed control are presented in Table A1 (see in Appendix A.2).

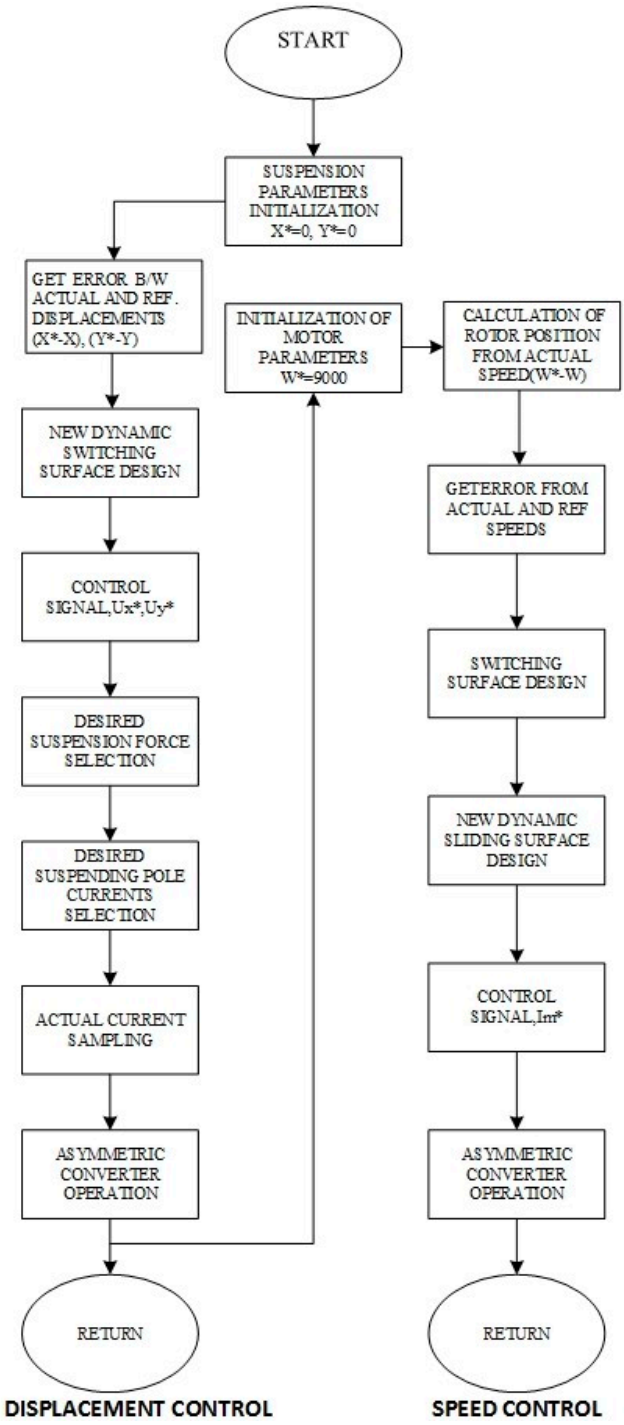

Figure 3. Stepwise flow chart for the implementation of the dynamic sliding mode control of the bearingless switched reluctance motor (BSRM).

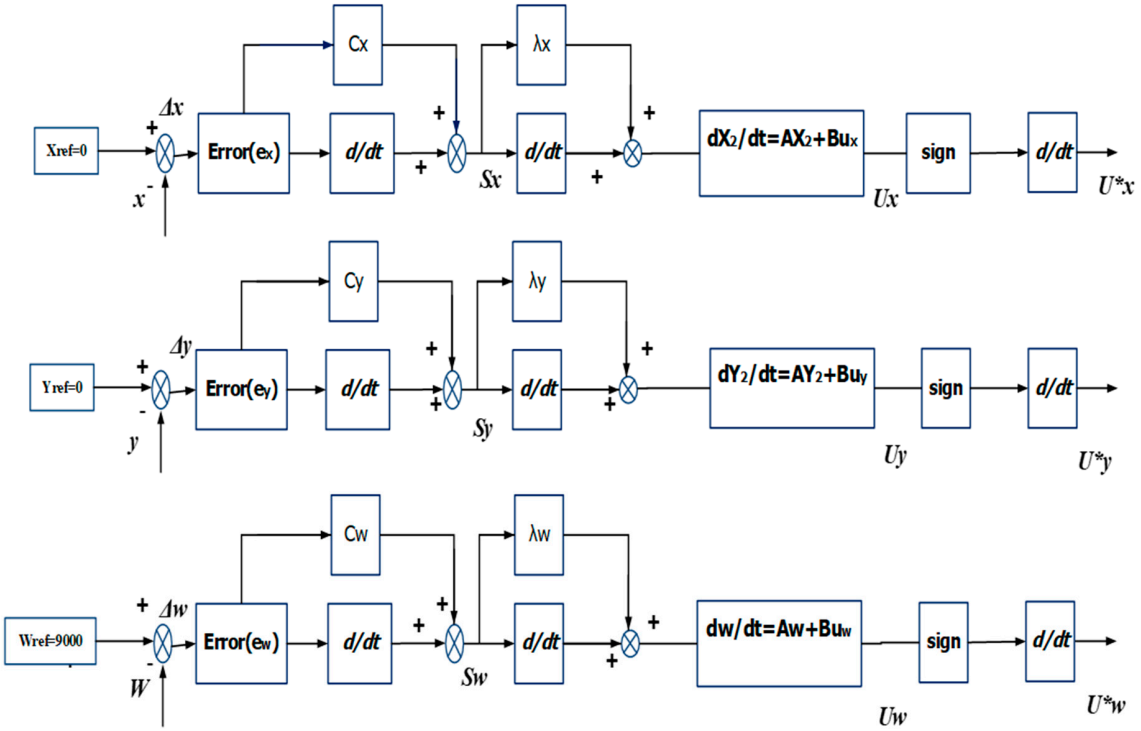

Figure 4. Block diagram of the dynamic sliding mode control.

3.2. Design of the SMO

The design parameters of the SMO are presented in Table A2 (see in Appendix A.3). The sliding mode observer states for the rotor displacements are modelled from individual suspension currents and voltages and are given in Equation (15):

$$\hat{\dot{X}}_2 = \frac{k}{m}x_1 + \mathrm{K}_x I_x + \mathrm{K}_y I_y + \mathrm{K}_{x2}\mathrm{sign}\left(\hat{I}_x - \mathrm{I}_x\right);\ \hat{\dot{Y}}_2 = \frac{k}{m}y_1 + \mathrm{K}_y I_y + \mathrm{K}_x I_x + \mathrm{K}_{y2}\mathrm{sign}\left(\hat{I}_y - \mathrm{I}_y\right) \quad (15)$$

Similarly, the motor equivalent observer state vectors' current, torque, flux linkages, speed and positions are modelled from the actual motor main winding phase voltages and currents, which are given collectively in Equations (16) to (20):

$$\hat{i} = \mathrm{N}(\hat{\theta})\hat{\psi} \quad (16)$$

$$\hat{T}_e = \hat{T}_e(\mathrm{i},\hat{\theta}) \quad (17)$$

$$\frac{d\hat{\psi}}{\mathrm{dt}} = -\mathrm{rN}(\hat{\theta})\hat{\psi} + \mathrm{V} + \mathrm{K}_\psi \mathrm{sign}(\hat{i} - \mathrm{i}) \quad (18)$$

$$\frac{d\hat{w}}{\mathrm{dt}} = \frac{\hat{\mathrm{Te}}}{J} - \frac{B}{J}\hat{w} + \mathrm{K}_w \mathrm{sign}(\hat{i} - \mathrm{i}) \quad (19)$$

$$\frac{d\hat{\theta}}{\mathrm{dt}} = \hat{w} + \mathrm{K}_\theta \mathrm{sign}(\hat{i} - \mathrm{i}) \quad (20)$$

From the above SMO equations, the notation ∧ indicates the measured value. The K_Ψ = 200, K_W = 30 and K_θ = 25 are the design parameters for the SMO, which are called the switching gain constants used as gain multipliers to the current error signal [21–23]. The equivalent structure of the sliding mode observer is shown in Figure 5. The sufficient condition of the sliding mode surface

($S^T \dot{S} \leq 0$) is considered to get the perfect system sliding mode property, even though under the presence of any faults. The switching dynamics are defined as shown in Equations (21) and (22):

$$S = \hat{i} - i = \begin{bmatrix} N_0 & 0 & M_0 \end{bmatrix} \begin{bmatrix} \hat{\psi} - \psi & \hat{w} - w & \hat{\theta} - \theta \end{bmatrix}^T \quad (21)$$

$$S = N_0 e_\psi + M_0 e_\theta, \ \dot{S} = N_0 \dot{e}_\psi + M_0 \dot{e}_\theta \quad (22)$$

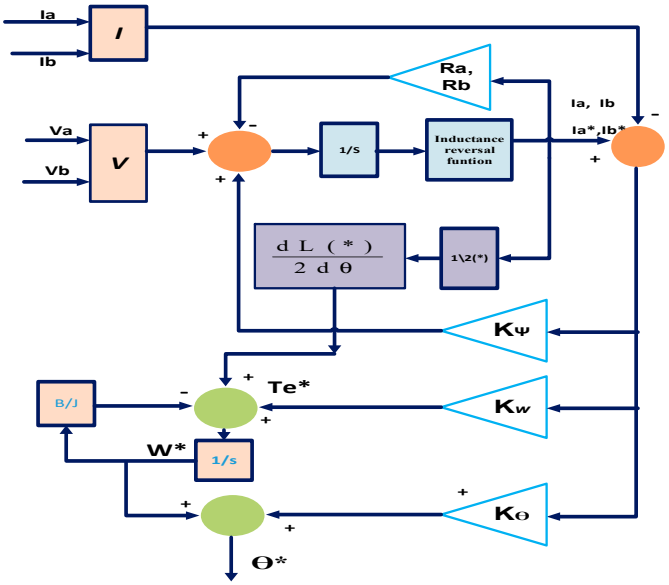

Figure 5. Block diagram of the sliding mode observer.

The detailed block diagram of the sensorless control BSRM is shown in Figure 6. The reference displacements are started at (0, 0), and the reference speed is fixed at 9000 rpm.

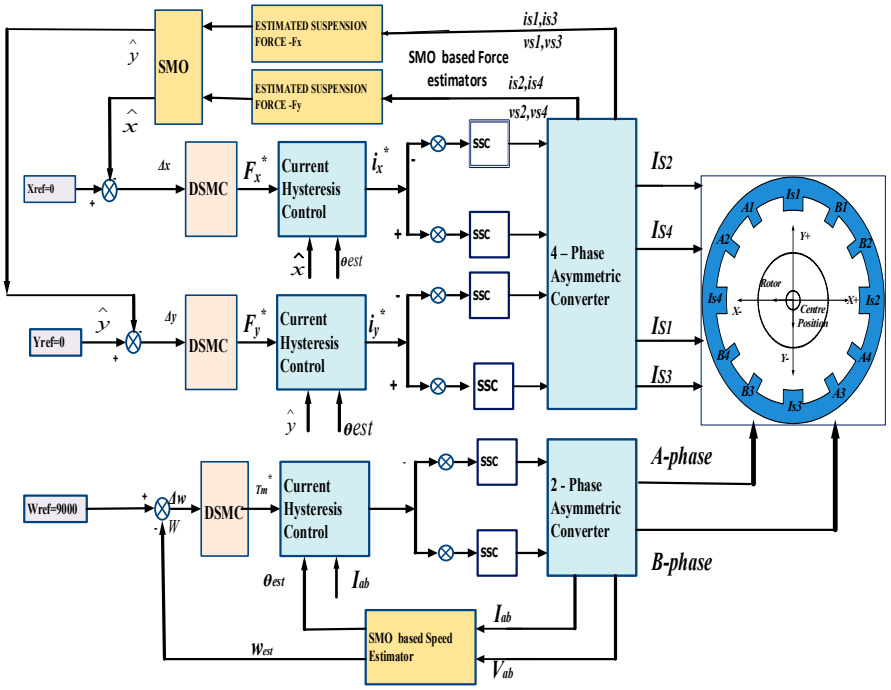

Figure 6. Overall sensorless control block diagram of the BSRM.

The resultant error signals are sent to the controller and generate the controlled command force signals of F_x * and F_y *. These command force signals are given to the current hysteresis control logic block, which excites the four-phase asymmetric converter. According to the generated current hysteresis control signals, the four-phase converter directs the controlled currents to the suspension windings. Finally, the controlled suspension magnetic force is produced, and it suspends the rotor to the centre position. The speed is calculated from the rotor position using the speed estimator block, which is further compared with the speed command W *(reference speed). The proposed controller in the speed loop produces the current command signal Im* according to the resultant speed error input signal. The current hysteresis control block generates the sign-enabled signals, which are applied to the two-phase asymmetric converter. This two-phase converter excites the stator main windings according to the control signals.

4. Results and Discussions

4.1. Measurements of the BSRM Parameters in Normal Conditions

The BSRM drive has started randomly with an initialised rotor position, but the sliding mode observer measures the rotor position nearly after 150 microsec. Figures 7–10 show the estimated and actual phase currents and current errors of both Phase–A and Phase-B windings, respectively. The differences between the measured and actual currents of both the phases are almost less than 0.05 amp, which means the measured currents are almost the same as the actual currents.

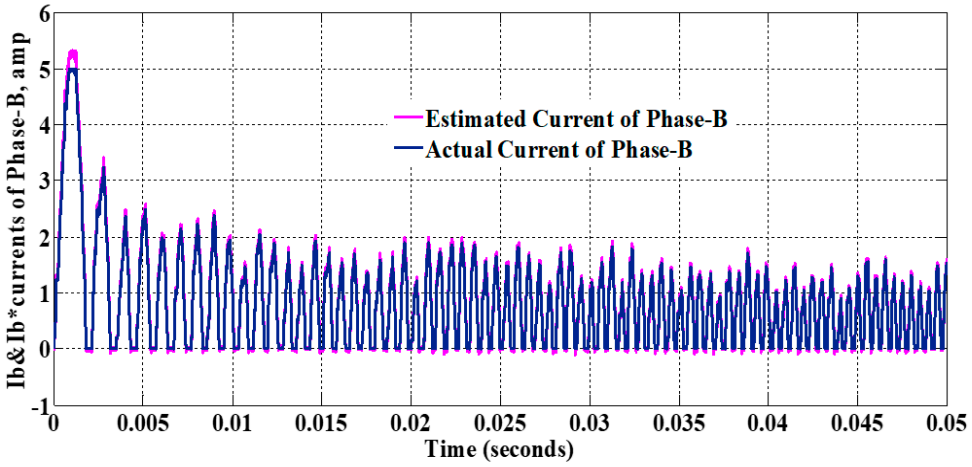

Figure 7. Estimated and actual phase-B currents.

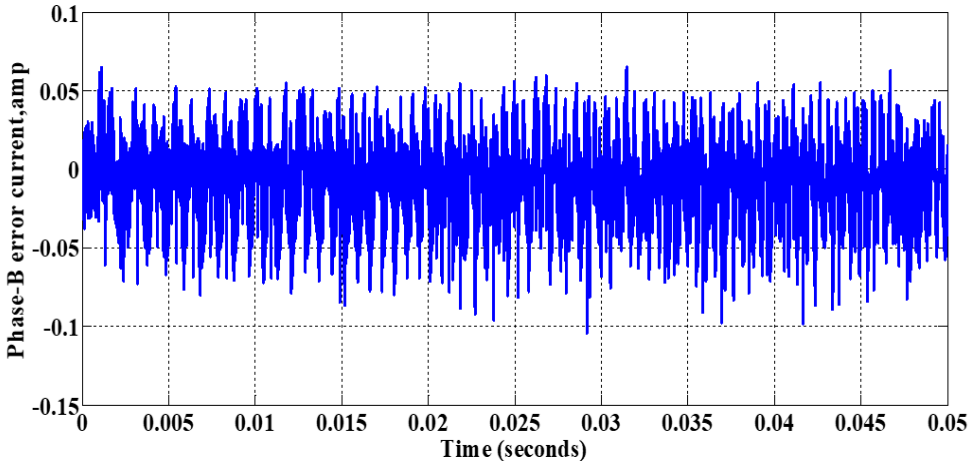

Figure 8. Error between the estimated and actual currents of phase-B.

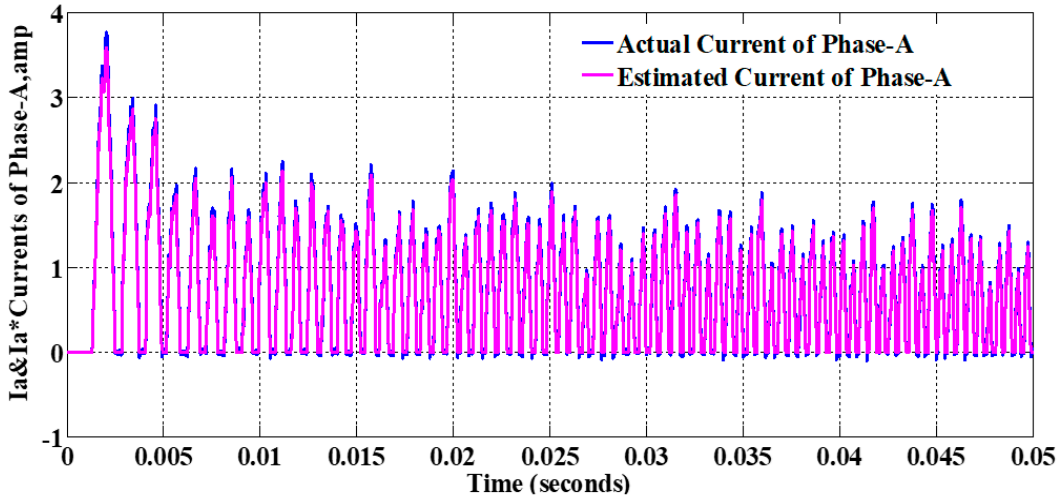

Figure 9. Estimated and actual phase-A currents.

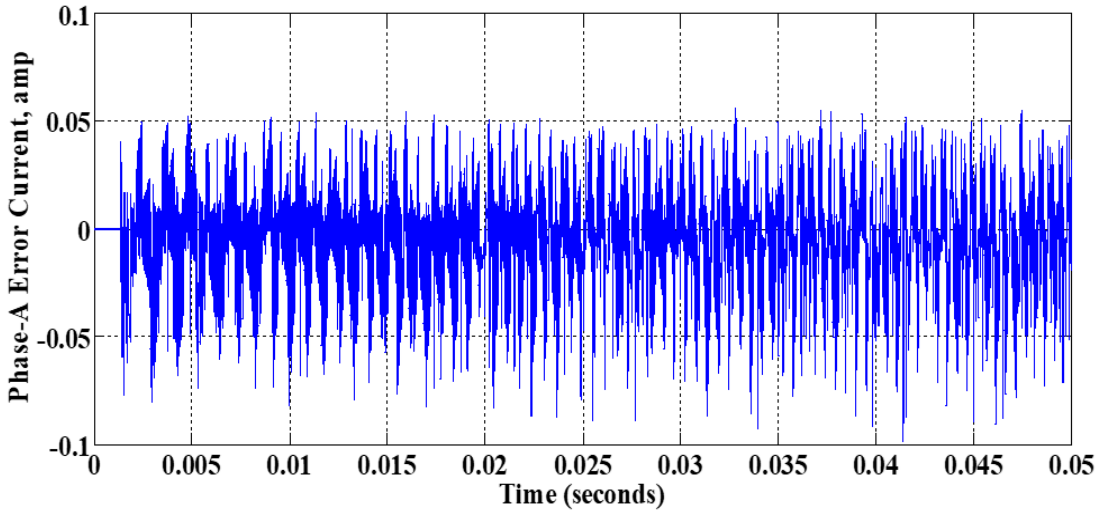

Figure 10. Error between the estimated and actual currents of phase-A.

Figures 11–14 show the actual and estimated suspension forces of both the X and Y directional windings, respectively. The actual and estimated suspension forces reached their steady states quickly, in less than 0.05 s only. Similarly, from Figures 13 and 14, it can be observed that the observer tracks the rotor positions in less than 0.0001 s for both phases. In Figure 15, the estimated and actual net torques are presented. From Figure 15, it is observed that the actual torque consists of both positive and negative ripples, because there is no technique that is employed to decrease the torque ripples in the actual system, but the observer's torque consists only of positive ripples and no more negative ripples due to the sensorless observer operation.

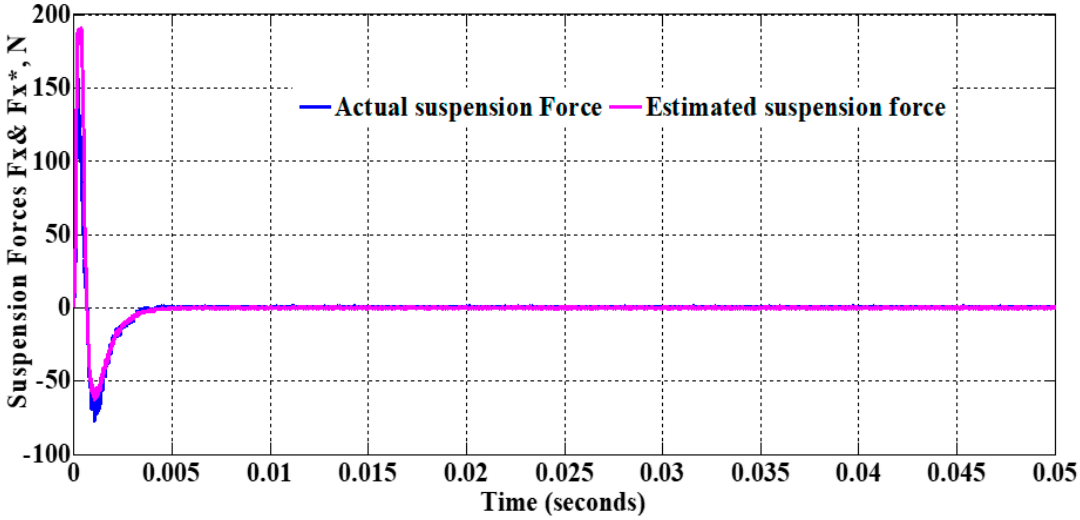

Figure 11. Actual and estimated X-directional suspension forces.

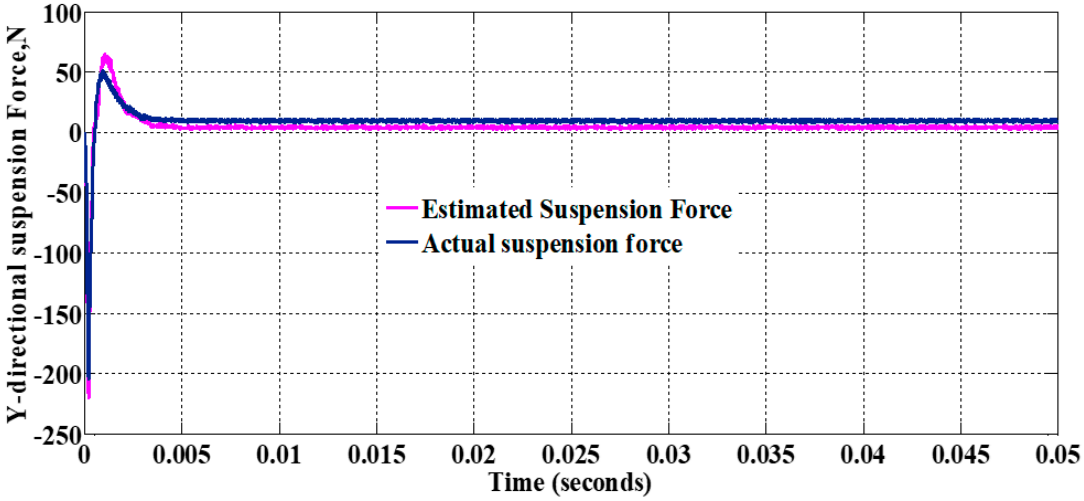

Figure 12. Estimated and actual Y-directional suspension forces.

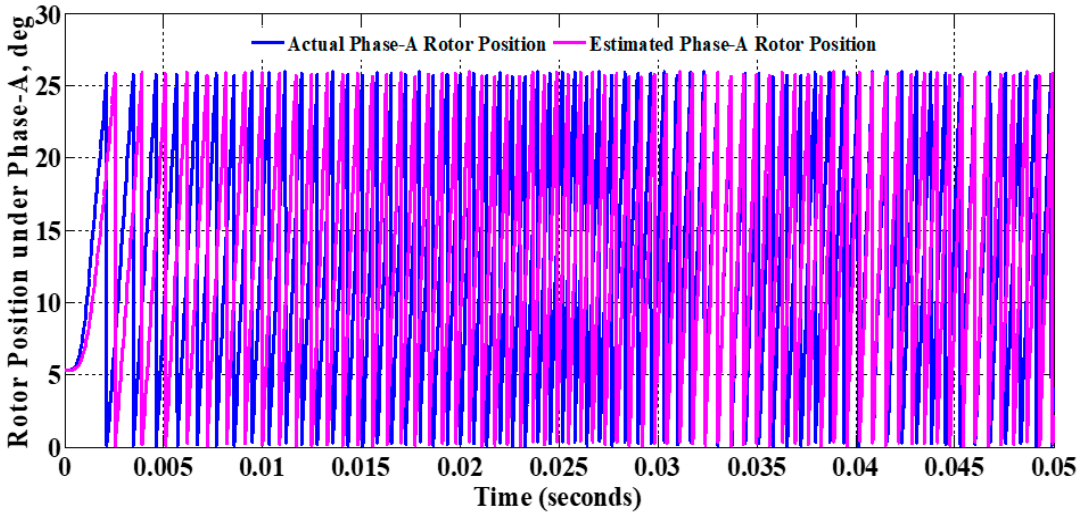

Figure 13. Estimated and actual rotor positions under phase-A.

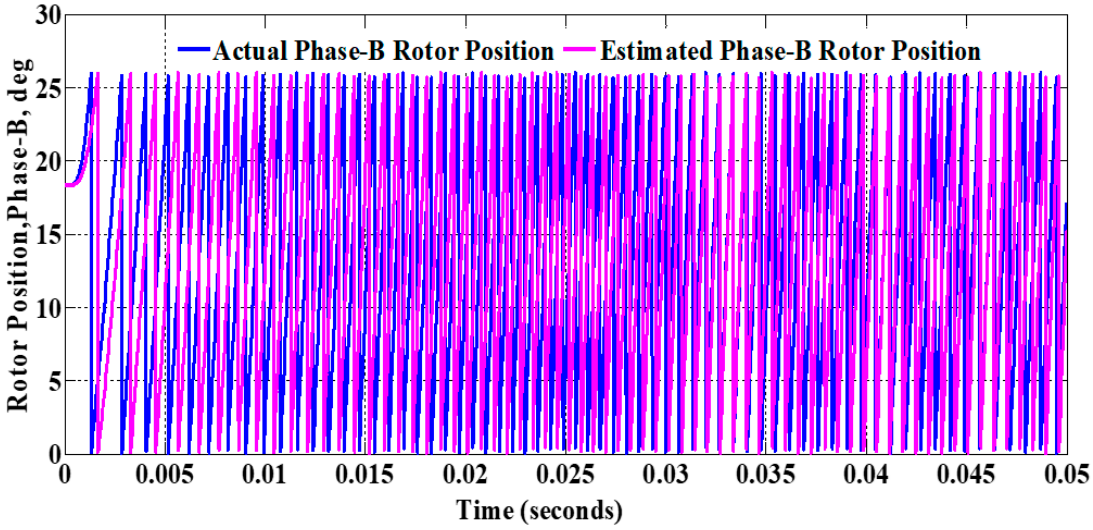

Figure 14. Estimated and actual rotor positions under phase-B.

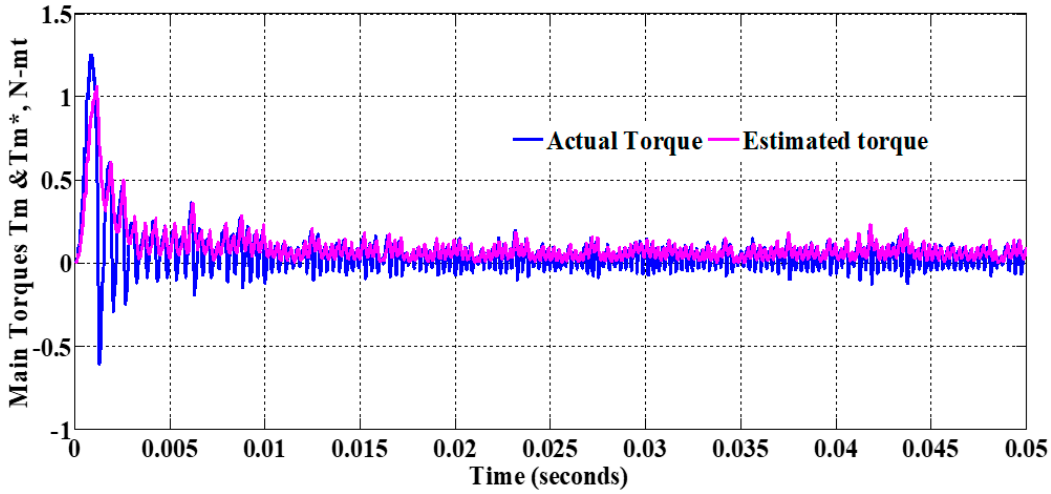

Figure 15. Estimated and actual net torques.

4.2. Suspension Control When There Is a Change in Suspension Loads

The fast-tracking and robustness properties of suspension parameters are verified and observed by increasing the suspension load of +10N at 0.02 s and removing it abruptly at 0.04 s. The actual and measured rotor displacement suspension forces are shown separately in Figure 16a–c, when the rotor is subjected to unexpected variations of the suspension loads. From Figure 16, it is clearly noticed that the proposed observer rapidly tracks the suspension forces, rotor displacements, in less than 0.003 s. The DSMC-based SMO suspended rotor parameters show the fast response in the transient period and stable robust behaviour at the steady-state conditions against the suspension loads.

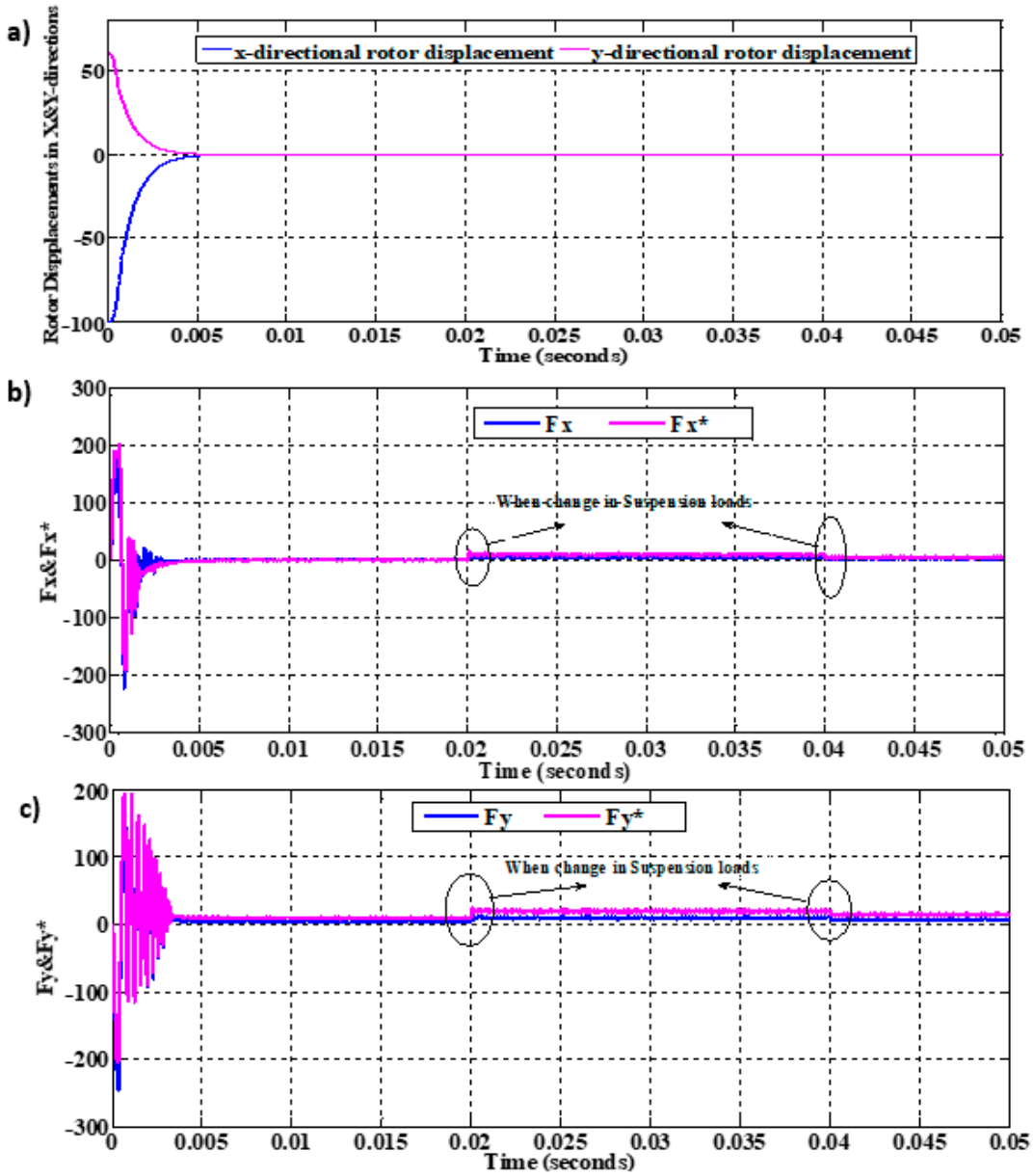

Figure 16. (**a**) Rotor X and Y displacements, (**b**) actual and estimated X-directional suspension forces when suspension loads are applied, and (**c**) actual and estimated Y-directional suspension forces when suspension loads are applied.

4.3. Sensorless Speed Control When the BSRM Is in Healthy Conditions

The observer rapidly tracks the speed in less than 0.001 s when the motor operated with a controlled current command of the proposed SMO at normal conditions. The actual and measured speeds of both the proposed controller-based SMOs are shown in Figure 17. From the figure, it can be observed that the speeds of the DSMC-based SMO reached their rated rpm in 0.01 s only. Hence, the DSMC-based SMO tracks the rated speed in less time due to the fast decaying exponential function in the switching surface.

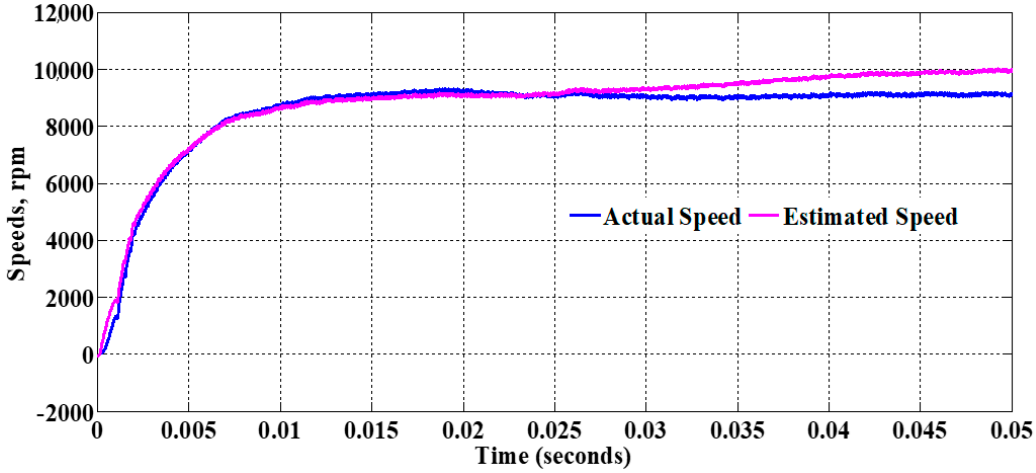

Figure 17. Estimated and actual speeds.

4.4. Sensorless Speed Control When Reference Speeds Are Changed

From Figure 18, the proposed observer maintains the stability and robustness in both the measured and actual speeds, even though there is an unexpected variation in the reference speeds: 9000 to 6000 rpm at 0.02 s and 6000 rpm to 9000 rpm at 0.04 s.

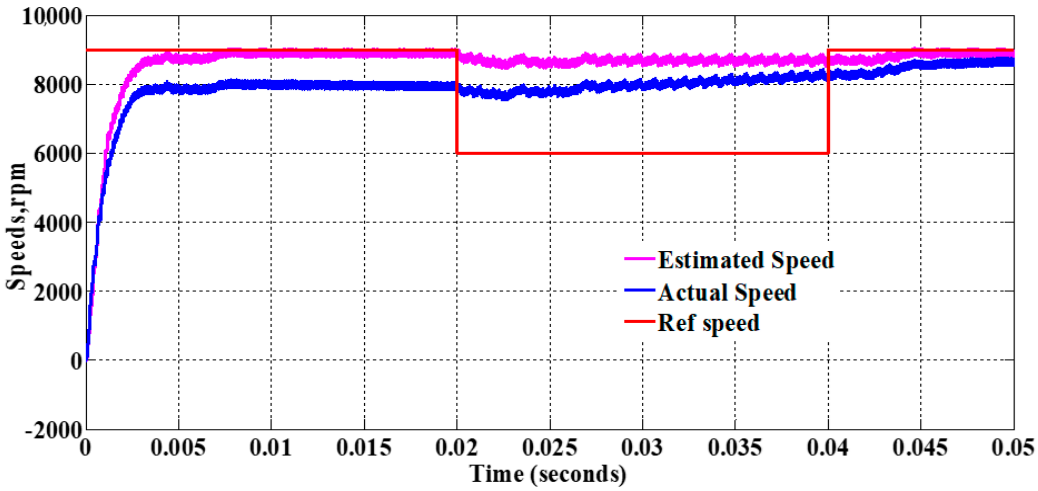

Figure 18. Estimated and actual speeds.

4.5. Sensorless Speed Control When There Is a Change of the Load Torque

In this case, the motor is loaded with 0.2 N-Mt load torque at 0.02 s and is disconnected suddenly at 0.04 sec. The actual and measured speeds of the observer, speed error tracking and actual and estimated net torque profiles are shown in Figure 19a–c, respectively. From the figures, it is noticed that there is a temporary increase in errors in the measured and actual speeds. From the speed and torque graphs, it can be understood that the measured rotor positions and speeds with the proposed controller-based SMO can be used for high-speed sensorless control applications.

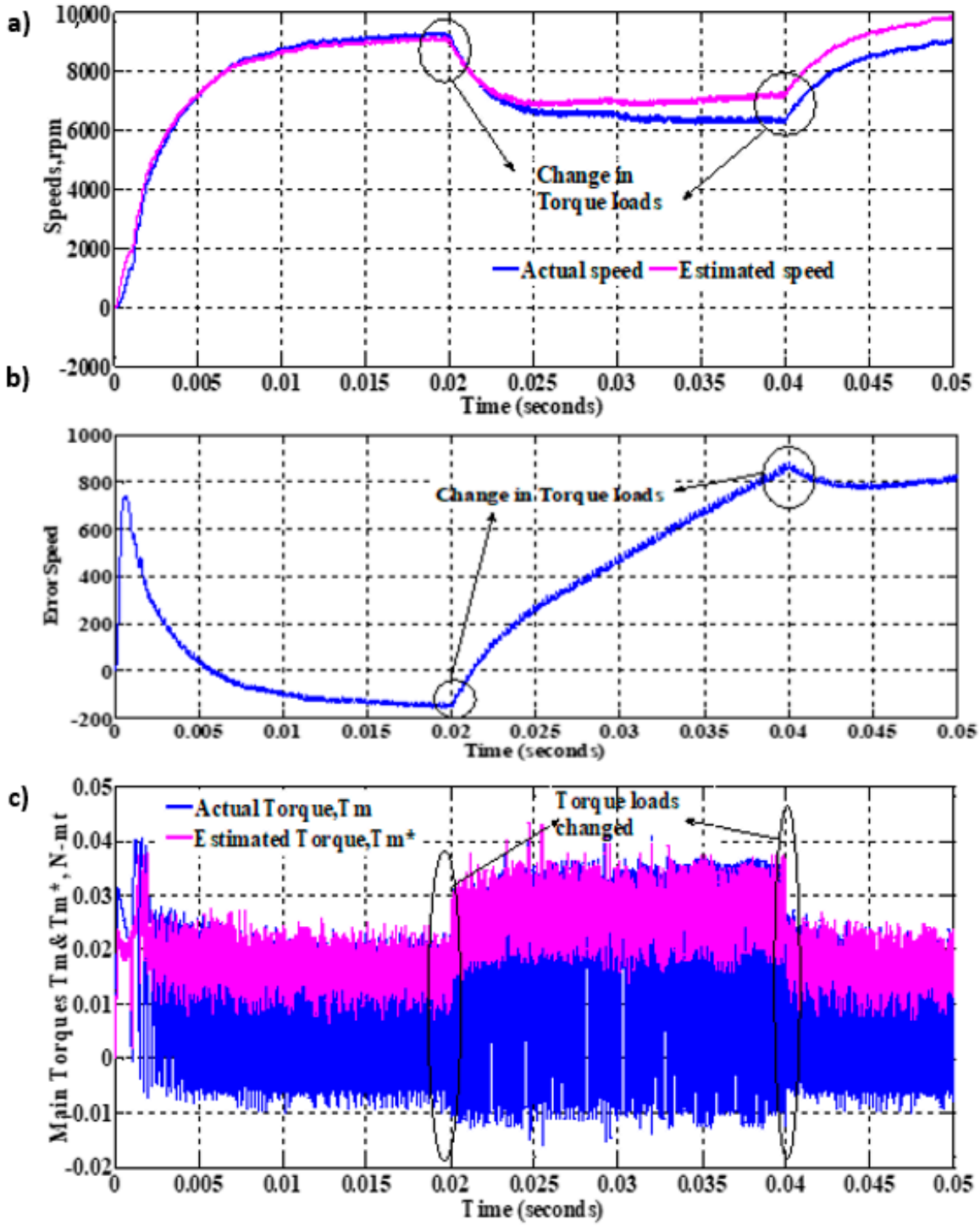

Figure 19. (**a**) Estimated and actual speeds, (**b**) speed tracking error, and (**c**) estimated and actual net torque values when load torques varied.

4.6. Sensorless Speed Control Change in the Moment of Inertia

The responses of the DSMC-based SMO under the sudden decrease and increase of the moment of inertia (10%) at 0.02 s are shown in Figure 20a–c, respectively. From these figures, it is observed that there is a little speed deviation in the estimated speed as related to the actual speed, which further illustrates the SMO's insensitivity and robustness.

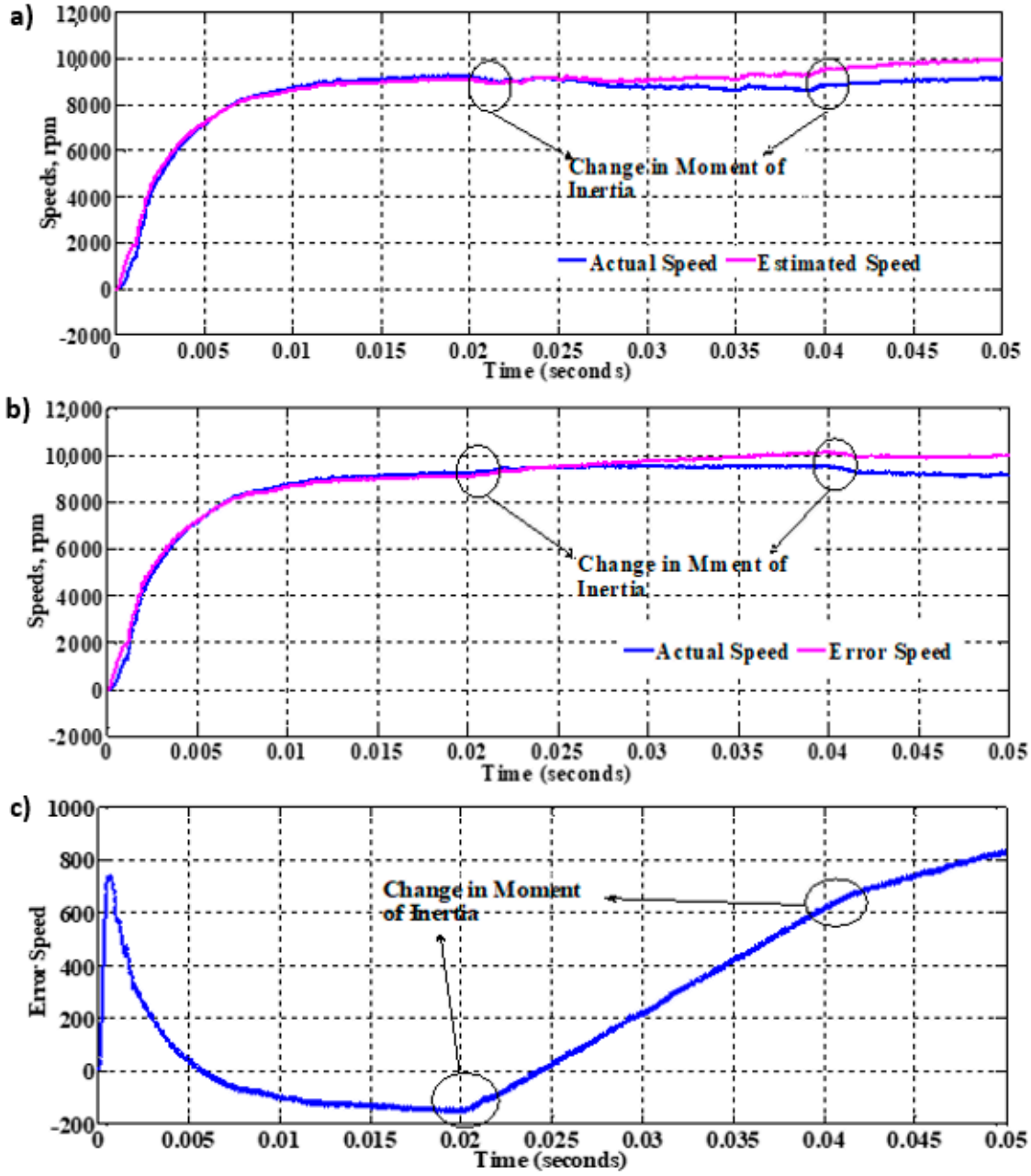

Figure 20. (**a**) Estimated and actual speeds when there are increments in the moment of inertia, (**b**) Estimated and actual speeds when there are decrements of the moment of inertia, and (**c**) Speed tracking error for change of the moment of inertia.

When the moment of inertia increased, the speed of the motor decreased. It is because that, with the increase in the moment of inertia, the phase current has to be increased to overcome the inertia, but the phase current is determined by the command current, and the command current is the proposition to the speed error with constant proposed controller parameters, according to the control schemes. Therefore, the speed decreased a little. Similarly, when the moment of inertia decreased, the speed of the rotor also increased.

4.7. Varying of the Supply Voltage and Phase Resistances

The DSMC-based SMO speed responses are shown in Figure 21a,b, when the supply voltage varies from 250 V to 200 V at 0.02 s and 200 V to 250 V at 0.04 s. The estimated speed responses do not change rapidly due to the proposed sliding mode controller and observer switching surface properties.

In the same way, the estimated speeds shown in Figure 21c are not much deviated with actual speed when the phase resistances are varied from 0.86 ohms to 0.43 ohms at 0.02 s and 0.43 ohms to 0.86 ohms at 0.04 s. Figure 21d shows the speed tracking error with the variations of the phase resistance.

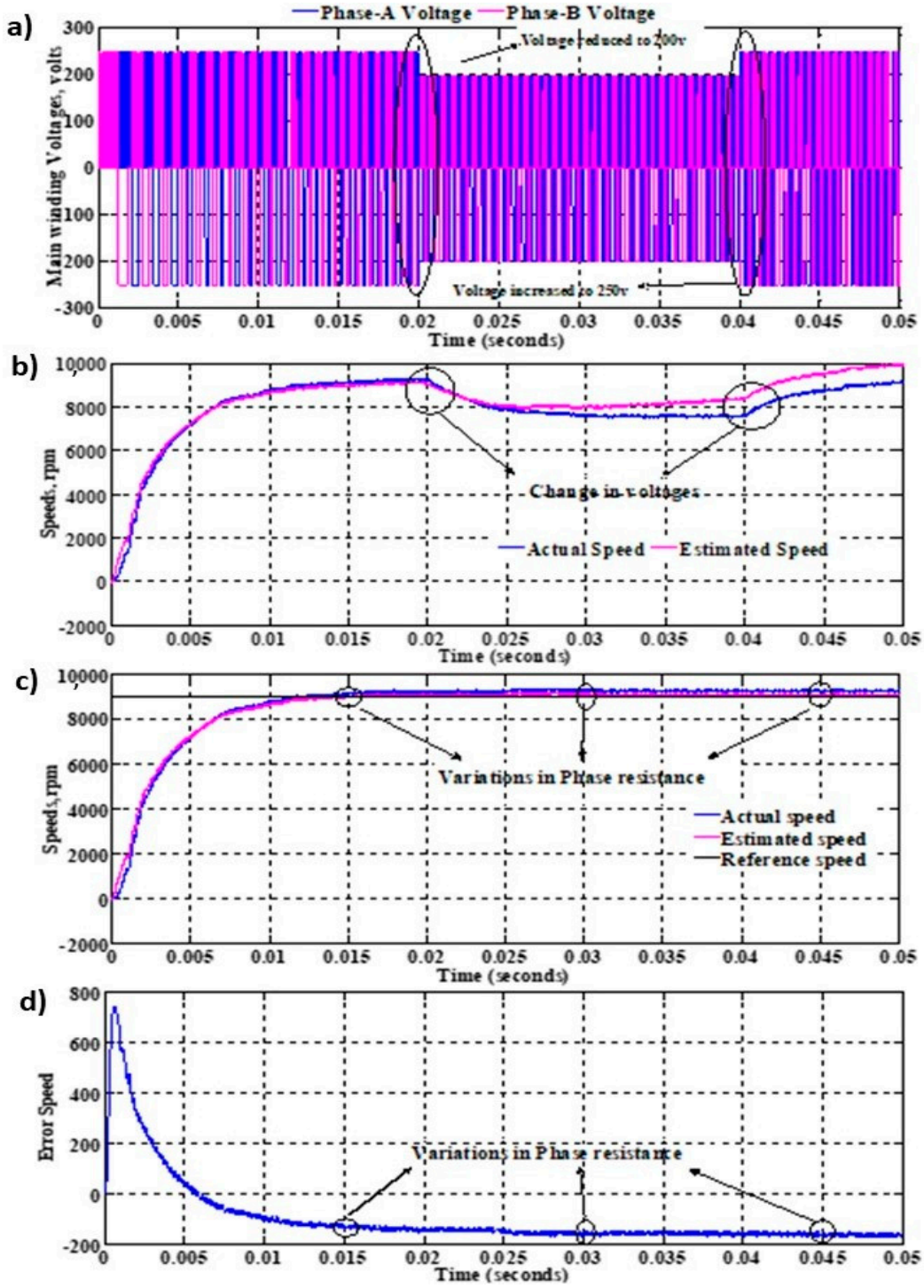

Figure 21. (**a**) Regulated main phase voltages, (**b**) estimated and actual speeds when changes in the supply voltage, (**c**) Estimated and actual speeds when changes in phase resistances, and (**d**) speed tracking error when the phase resistances are varied.

4.8. Sensorless Speed Control When There Are Changes in the Switching Angle

The estimated and actual speeds responses are shown in Figure 22a,b, with the changes of the switching angles to 11 degrees and 13 degrees, respectively, at 0.02 s. The observer estimated speeds almost approach the reference speeds, even though the change of the switching angles, but the actual speed, deviates quietly. The speed-tracking error graphs for both cases are also shown in Figure 23a,b.

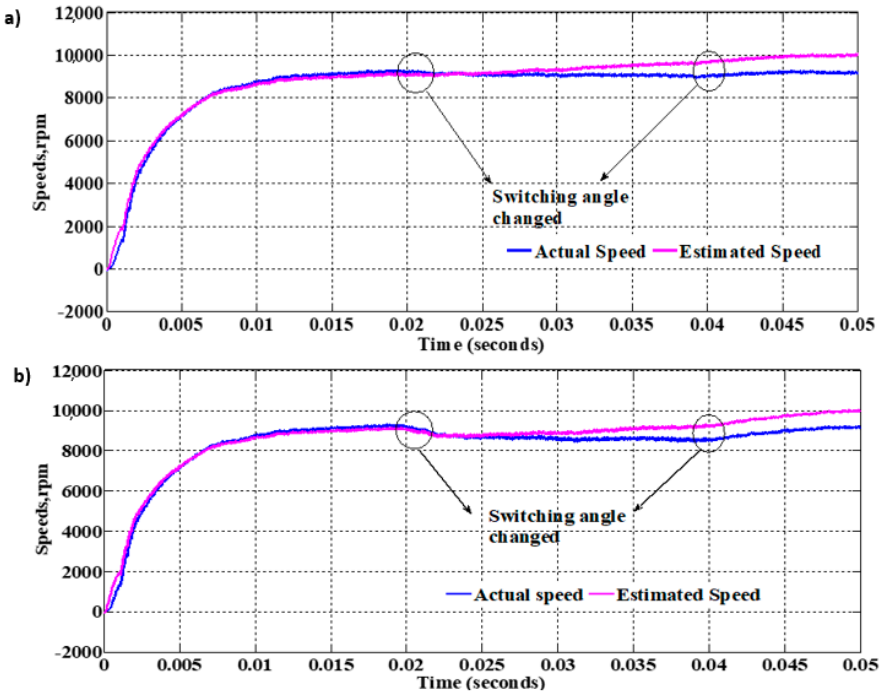

Figure 22. (**a**) Estimated and actual speeds when switching angle is changed to 11 degrees and (**b**) Estimated and actual speeds when switching angle is changed to 13 degrees.

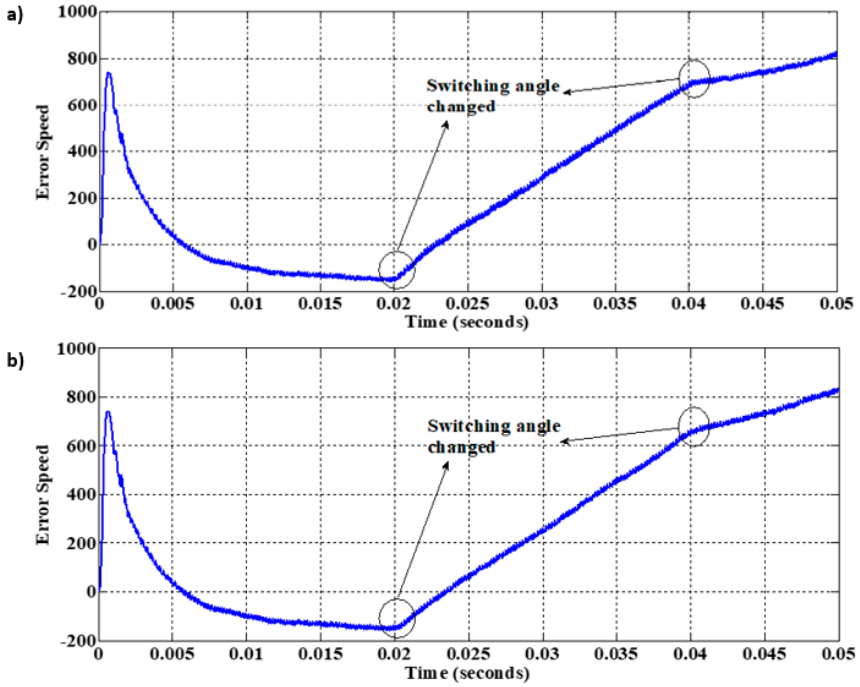

Figure 23. (**a**) Speed-tracking error when switching angle is changed to 11 degrees (**b**) Speed-tracking error when switching angle is changed to 13 degrees.

From all the above conditions, the DSMC-based sliding mode observer offers fast and accurate measurements of the rotor position and speed at the time of starting, as compared with the DSMC-based SMO. The good thing observed in the proposed observer is that it offers a robust performance and less chattering, even under a sudden change in the electrical or mechanical parameters.

5. Comparisons of Speeds with the Conventional SMC-Based SMO

Figures 24–29 show the comparison results of the conventional SMC and proposed DSMC-based sliding mode observers offering stable speed measurements when the BSRM was subjected to different electrical and mechanical parameter variations. The actual and estimated speeds of the DSMC-based SMO converge on the desired speed (9000 rpm) at 0.01 s, and conventional SMC-based SMO converges at 0.008 s. Even though the SMC-based SMO method has a less settling time than the DSMC-based SMO, it suffers from high chattering and significant steady-state errors. In the case of the DSMC-based SMO method, the chattering phenomena was reduced to a very lesser extent, which shows a smooth and strong robustness against all parameter variations and less steady-state errors.

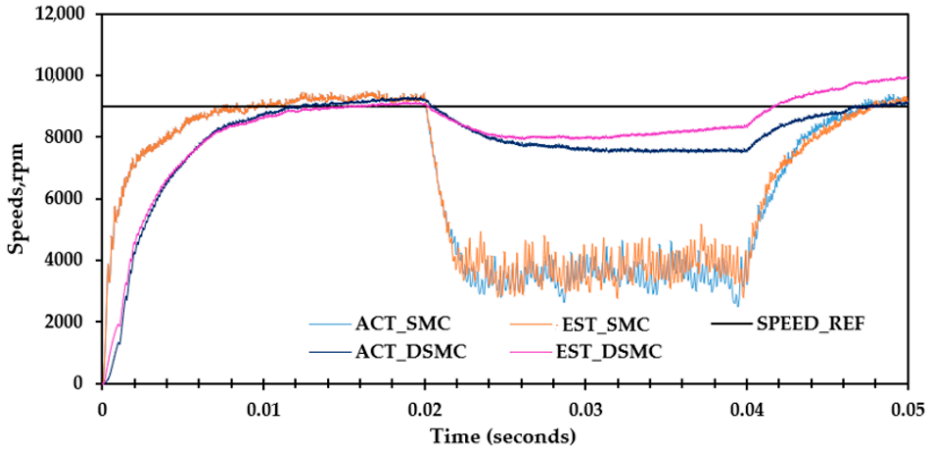

Figure 24. Changes in the supply voltage. [Note: ACT_SMC: actual speed under sliding mode controller; EST_SMC: estimated speed under sliding mode controller; ACT_DSMC: actual speed under dynamic sliding mode controller; EST_DSMC: estimated speed under dynamic sliding mode controller; SPEED_REF: reference speed].

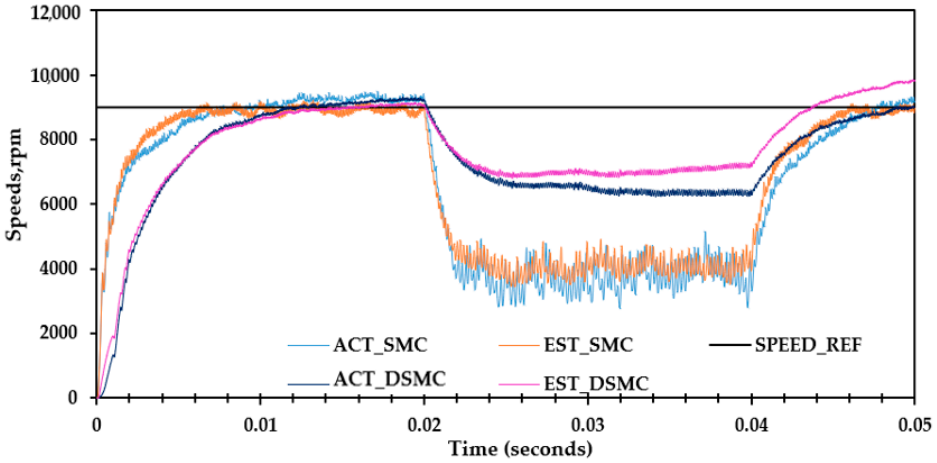

Figure 25. Changes in the load torque. [Note: ACT_SMC: actual speed under sliding mode controller; EST_SMC: estimated speed under sliding mode controller; ACT_DSMC: actual speed under dynamic sliding mode controller; EST_DSMC: estimated speed under dynamic sliding mode controller; SPEED_REF: reference speed].

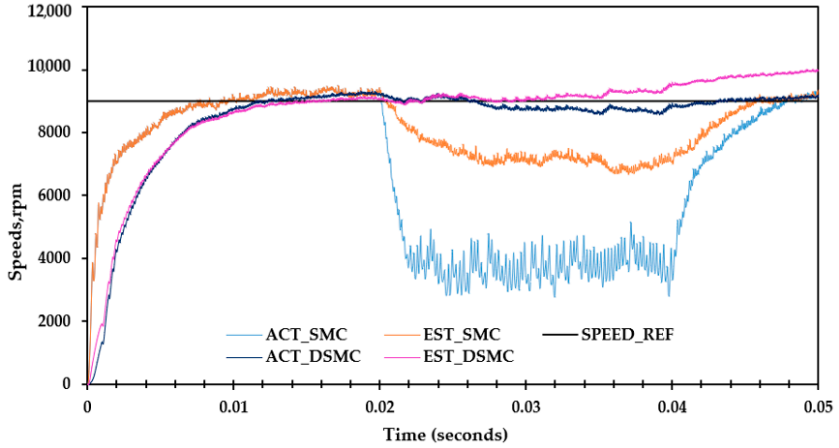

Figure 26. Increments of the moment of inertia by 10%. [Note: ACT_SMC: actual speed under sliding mode controller; EST_SMC: estimated speed under sliding mode controller; ACT_DSMC: actual speed under dynamic sliding mode controller; EST_DSMC: estimated speed under dynamic sliding mode controller; SPEED_REF: reference speed].

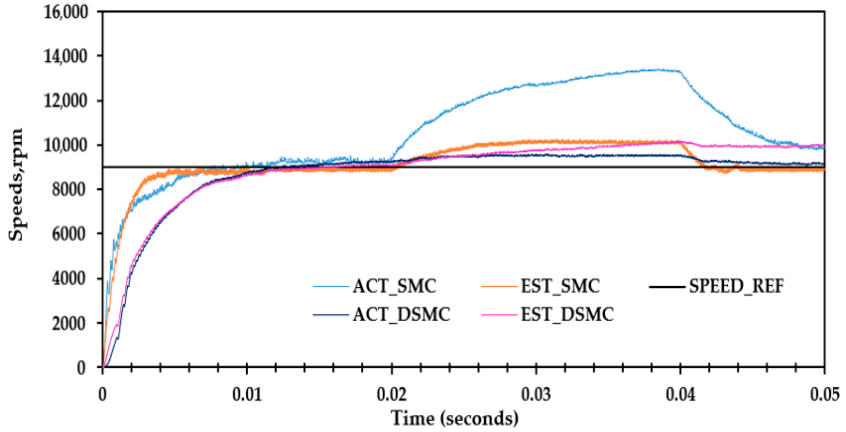

Figure 27. Decrements of the moment of inertia by 10%. [Note: ACT_SMC: actual speed under sliding mode controller; EST_SMC: estimated speed under sliding mode controller; ACT_DSMC: actual speed under dynamic sliding mode controller; EST_DSMC: estimated speed under dynamic sliding mode controller; SPEED_REF: reference speed].

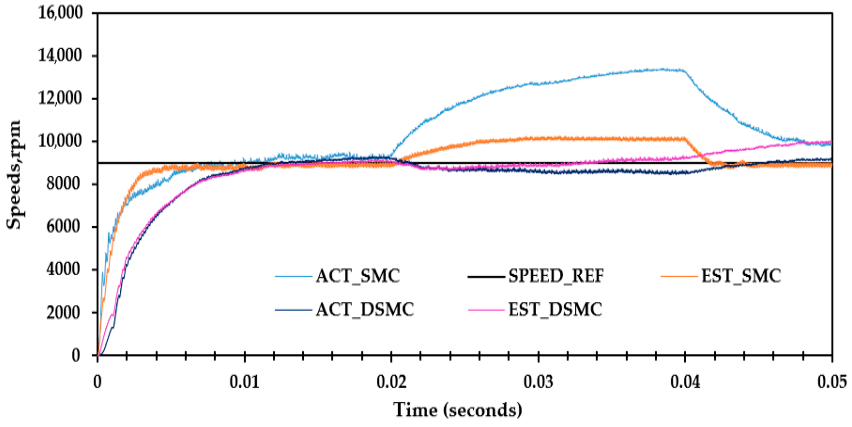

Figure 28. Changes in the switching angle to 11 degrees. [Note: ACT_SMC: actual speed under sliding mode controller; EST_SMC: estimated speed under sliding mode controller; ACT_DSMC: actual speed under dynamic sliding mode controller; EST_DSMC: estimated speed under dynamic sliding mode controller; SPEED_REF: reference speed].

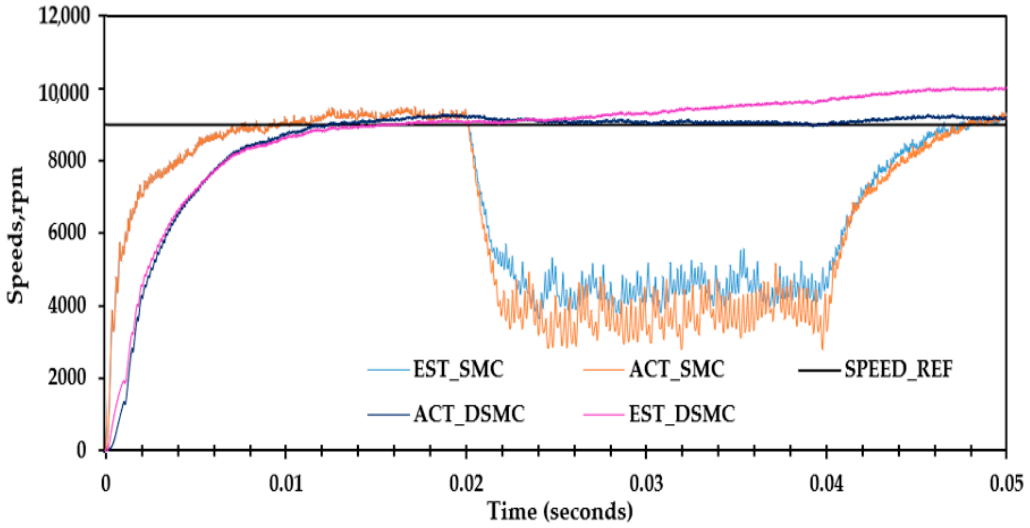

Figure 29. Change in the switching angle to 13 degrees. [Note: ACT_SMC: actual speed under sliding mode controller; EST_SMC: estimated speed under sliding mode controller; ACT_DSMC: actual speed under dynamic sliding mode controller; EST_DSMC: estimated speed under dynamic sliding mode controller; SPEED_REF: reference speed].

The overall speed performance comparison of the SMC-based SMO and DSMC-based SMO is presented in Table 4.

Table 4. Comparisons of speeds between the proposed and conventional methods.

Parameters	SMC Based-SMO		DSMC-Based SMO	
Change of system parameters	Difference in speed	% of Chattering	Difference in speed	% of Chattering
Change of Switching angle to 13 degree	3000	±8	1000	±3
Varying of supply voltage	3500	±8	1500	±5
Varying in load Torque	3500	±8	1500	±5
Decrease of moment of inertia by 10%	3000	±5	800	±4
Increase of moment of inertia by 10%	2000	±5	800	±4
Change of Switching angle to 11 degree	2000	±8	1000	±3

Note: SMC-sliding mode controller; DSMC-dynamic sliding mode controller; SMO-sliding mode observer

6. Conclusions

In this paper, a novel sensorless DSMC-based sliding mode observer is proposed to achieve a reliable and smooth start. It was demonstrated that, with the proposed method, the motor can start promptly from any arbitrary initial position. The starting was achieved without an initial jerk. At higher speeds, the accuracy of the speed and displacement measurements of the DSMC-based SMO are reasonably good (within ±2%). The chattering phenomena were reduced to a minimal extent and tracked the speed in less than 0.005 s only. The sensorless DSMC-based SMO gave accurate rotor displacement, position and speed measurements with any sudden change of loading conditions and reference values, as compared with the SMC-based SMO. Hence, the DSMC-based SMO method is very suitable for the sensorless control of the BSRM at higher speeds with any consideration of internal and external disturbances.

Author Contributions: Data curation, P.N.R.; formal analysis, P.N.R. and N.M.K.; funding acquisition, S.P. (towards APC); methodology, P.N.R. and N.M.K.; resources, S.P.; software, P.N.R.; visualisation, N.M.K.; writing—original draft, P.N.R. and N.M.K. and writing—review and editing, P.N.R., N.M.K., S.P, M.S.P.S. and A.A.C. All authors have read and agreed to the published version of the manuscript.

Funding: This research received no external funding.

Acknowledgments: We authors acknowledge the Department of Energy Technology, Aalborg University, Esbjerg, Denmark for sharing technical experts.

Conflicts of Interest: The authors declare no conflict of interest.

Nomenclature

m	Rotor weight in kg
g	Gravitational force
Fx, Fy	Suspension forces, N
F_{dx}, F_{dy}	Uncertain disturbances, N
K_X, K_Y	Equivalent constant matrices of suspension forces
K_{xxp}, K_{yyp} K_{xyp}, K_{yxp}, K_{xxn}, K_{yyn}, K_{xyn}, K_{yxn}	Equivalent suspension force constants in both positive and negative directions, respectively
I_x,I_Y	Suspension current vectors
ixp, iyp, ixn, iyn	X and Y-directional individual suspension currents
ψ	Per phase flux linkages
r	Phase resistance, ohms
N	Phase-inductance reversal vector
N_0, M_0	Initial reversal flux and position vector constants, respectively
θ	Position of the rotor per phase in degree
V	Phase voltage vector, volts
w	Speed of the rotor, rpm
T_e, T_l	Net actual torque and applied load torque
B, J	Damping coefficient, actual moment of inertia of rotor
i	Main phase current vector, amps
X_{ref}, Y_{ref}, X_d, Y_d	Rotor reference and desired displacements
X_2,Y_2, $\hat{X}_2$,$\hat{Y}_2$	Actual and estimated rotor displacements
K_ψ,K_w,K_θ	Flux linkage, speed and position observer coefficients
e_x, e_y, e_w, e_ψ, e_θ	Displacement errors, error speed, flux linkage and positions, respectively
C_x, C_y, C_w	Rotor X and Y displacements and speed-switching function positive constants, respectively
S_x, S_y, S_w	Rotor X and Y displacements and speed-sliding mode switching equations, respectively
U_x, U_y, U_w	Rotor X and Y displacements and speed control equations, respectively
σ_x, σ_y, σ_w	New dynamic sliding mode switching constants of rotor displacements and speed, respectively
λ_x, λ_y, λ_w	Rotor displacements and speed control design constants
η_x, η_y, η_w	Signum function constants

Appendix A

Appendix A.1. Asymmetric Converter

Due to many advantages, such as the capability of independent control for each phase and four switching modes, asymmetric converters are adopted for suspending force windings and torque windings, respectively. The topology of the asymmetric converter circuit is shown below in Figure A1.

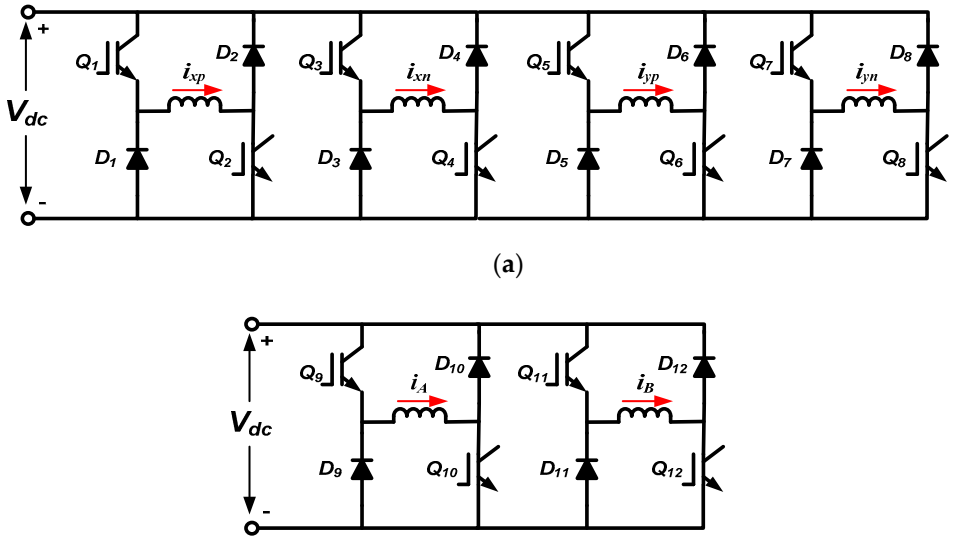

Figure A1. (**a**) Asymmetric converter for torque windings. (**b**) Asymmetric converter for suspending force windings.

Appendix A.2. DSMC Controller Design Parameters

The DSMC controller design parameters are presented in Table A1.

Table A1. DSMC design parameters.

Parameters	Values
Cx, λx, ηx	5, 20, 78
Cy, λy, ηy	15, 20, 108
Cw, λw, ηw	10, 15, 130

Note: DSMC-dynamic sliding mode controller

Appendix A.2.1. Design of Switching the Function Constant

The switching function is given by $S(x) = C^T X$, where $C = [C_1, C_2, \ldots, C_n]$, and C should be selected so that the polynomial $P^{n-1} + (c_{n-1})\left(P^{n-2}\right) + \ldots + (c_2)(P) + c_1$ is a Hurwitz polynomial, where P is a Laplace operator.

Let the X and Y-axis dynamics be:

$$\dot{X}_1 = X_2 \; ; \; \dot{Y}_1 = Y_2$$

$$\dot{X}_2 = -\frac{k_x}{m}X_1 + \frac{F_x}{m} + F_{dx} \; ; \; \dot{Y}_2 = -\frac{k_y}{m}Y_1 + \frac{F_y}{m} + F_{dy} + g$$

Here, the number of states, i.e., $n = 2$, so that $S(x) = c_x X_1 + X_2$; to satisfy the condition that the polynomial $P + c_x$ is Hurwitz, the Eigen value of $(P + c_x) = 0$ should have a negative real part, i.e., $c_x > 0$.

Based on the above condition, we performed a simulation study with the proper tuning of values for c_x, c_y and c_w. After an extensive tuning, the desired response was obtained for the values provided in Table A1.

Appendix A.2.2. Design of the new switching function constant

When $\sigma_x = 0$ and $\sigma_y = 0$, the new switching characteristic equations become as follows:

$\dot{S}_x + \lambda_x S_x = 0$ and $\dot{S}_y + \lambda_y S_y = 0$.

Therefore, λ_x and λ_y must be real positive constants to get a stable condition (Routh-Hurwitz criteria).

The conditions for designing the constants are:

(a) $\dot{\sigma}\sigma = \sigma\left(\dot{D}(t) + (c + \lambda D(t) - \eta \mathrm{sgn}(\sigma)\right)$, where σ, D and η are the dynamic switching mode, uncertain function and signum function constants, respectively.

(b) $\eta > D + (c + \lambda)(D_0)$, where D_0 is initial value of the uncertain function constant.

Hence, the new dynamic switching surface design constants are obtained after proper tuning until the desired response is achieved. The values are given in Table A1.

Appendix A.3. SMO Controller Design Parameters

The SMO controller design parameters are presented in Table A2.

Table A2. SMO design parameters.

SMO Design Parameters	Values
Kx2, Ky2	250, 400
K_Ψ	200
K_w	30
K_θ	25

Note: SMO-sliding mode observer.

References

1. Bosch, R. Development of a Bearing-less Electric Motor. In Proceedings of the International Conference on Electric Machines (ICEM'88), Pisa, Italy, March 1988; pp. 373–375.
2. Bichsel, J. The Bearing-less Electrical Machine. In Proceedings of the International Symposium on Magnetic Suspension Technology, NASA Langley Res. Center, Hampton, VA, USA, 19–23 August 1991; pp. 561–573.
3. Morrison, C.R.; Siebert, M.W.; Ho, E.J. Electromagnetic Forces in a Hybrid Magnetic-Bearing Switched-Reluctance Motor. *IEEE Trans. Magn.* **2008**, *44*, 4626–4638. [CrossRef]
4. Takemoto, M.; Shimada, K.; Chiba, A. A Design and Characteristics of Switched Reluctance Type Bearing less Motors. In Proceedings of the 4th International Symposium on Magnetic Suspension Technology, Gifu, Japan, 30 October–1 November 1997; pp. 49–63.
5. Takemoto, M.; Chiba, A.; Fukao, T. A New Control Method of Bearing-less Switched Reluctance Motors Using Square-wave Currents. In Proceedings of the IEEE Power Engineering Society, Singapore, Singapore, 23–27 January 2000; pp. 375–380.
6. Takemoto, M.; Suzuki, H.; Chiba, A. Improved Analysis of a Bearing less Switched Reluctance Motor. *IEEE Trans. Ind. Appl.* **2001**, *37*, 26–34. [CrossRef]
7. Liu, J.; Wang, X. *Advanced Sliding Mode Control for Mechanical Systems*; Springer: Berlin/Heidelberg, Germany, 2011.
8. Koshkouei, A.J.; Burnham, K.; Zinober, A. Dynamic Sliding Mode Control Design. *IEE Proc. Control Theory Appl.* **2005**, *152*, 392–396. [CrossRef]
9. Sarah, K.S. Sliding mode observers a survey. *Int. J. Syst. Sci.* **2008**, *39*, 751–764.
10. Roy, A.M.; Mohammad, S.I.; Hussain, I. Application of a sliding mode observer for Position and Speed Estimation in Switched Reluctance Motor drive. *IEEE Trans. Ind. Appl.* **2001**, *37*, 51–58.
11. Khalid, N.; Attaullah, Y.M. Output Feedback Control of a Class of Under-Actuated Nonlinear Systems Using Extended High Gain Observer. *Arab. J. Sci. Eng.* **2016**, *41*, 3531–3542. [CrossRef]
12. Wang, H.J.; Lee, D.H.; Ahn, J.W. Novel Bearing less Switched Reluctance Motor with Hybrid Stator Poles: Concept, Analysis, Design and Experimental Verification. In Proceedings of the International Conference on Electrical. Machines and Systems, Wuhan, China, 17–20 October 2008; pp. 3358–3363.
13. Lee, D.; Ahn, J. Design and Analysis of Hybrid Stator Bearing less SRM. *J. Electr. Eng. Technol.* **2011**, *6*, 94–103. [CrossRef]
14. Wang, H.; Wang, Y.; Liu, X.; Ahn, J.W. Design of novel bearing-less switched reluctance motor. *IET Electr. Power Appl.* **2012**, *6*, 73–81. [CrossRef]
15. Yang, Y.; Zhang, Y. Sliding mode-PI control of switched reluctance motor drives for EV. In Proceedings of the 2005 International Conference on Electrical Machines and Systems, Nanjing, China, 27–29 September 2005; Volume 1, pp. 603–607.
16. Edwards, C.; Spurgeon, S. Robust output tracking using a sliding mode controller /observer scheme. *Int. J. Control* **1996**, *64*, 967–983. [CrossRef]
17. Edwards, C.; Spurgeon, S. *Sliding Mode Control: Theory and Applications*; Taylor & Francis: London, UK, 1998.

18. Utkin, V.; Guldner, J.; Shi, J. *Sliding Mode Control in Electro-Mechanical Systems*; Taylor & Francis: London, UK, 1999.
19. Gholipour, S.; Shandiz, H. Dynamic Sliding Mode Control based on Fractional calculus subject to uncertain delay based chaotic pneumatic robot. *arXiv* **2013**, arXiv:1309.7666v3. [CrossRef]
20. Alan, S.I. Zinober, Discussion on Dynamic Sliding Mode Control for a Class of Systems with Mismatched Uncertainty. *Eur. J. Control* **2005**, *11*, 11–18.
21. Vieira, R.P.; Gastaldini, C.C.; Azzolin, R.Z.; Gründling, H.A. Discrete-time sliding mode speed observer for sensor-less control of induction motor drives. *IET Electr. Power Appl.* **2012**, *6*, 681–688. [CrossRef]
22. Zhan, Y.J.; Chan, C.C.; Chau, K.T. A novel sliding-mode observer for Indirect sensing of Switched reluctance Motor drives. *IEEE Trans. Ind. Appl.* **1999**, *46*, 390–397. [CrossRef]
23. Mohammad, S.I.; Hussain, I.; Veillette, R.J.; Batur, C. Design and performance analysis of sliding mode observers for sensor less operation of switched reluctance motors. *IEEE Trans. Ind. Appl.* **2003**, *3*, 383–389.